JOURNAL OF GEOPHYSICAL RESEARCH, VOL. 111, D14207, doi:10.1029/2005JD006968, 2006

Thermodynamic, cloud microphysics, and rainfall responses to initial moisture perturbations in the tropical deep convective regime

Xiaofan Li,[1] Shunli Zhang,[2] and Da-Lin Zhang[2]

Received 8 December 2005; revised 28 February 2006; accepted 5 April 2006; published 22 July 2006.

[1] In this study, the precipitable water (PW) and ice water path (IWP) simulated by the Global Data Assimilation System (GDAS) are compared to those observed by NOAA's Microwave Surface and Precipitation Products System. Results show small root-mean-square (RMS) differences in PW but large RMS differences in IWP between the two data sets, indicating the existence of model errors in reproducing clouds. To examine the possible linkage between the small PW and large IWP differences, three experiments are conducted with a two-dimensional cloud-resolving model in which the observed zonal wind and the GDAS-derived large-scale vertical velocity are imposed. The model initial conditions of PW are perturbed by ±10% in the first two experiments, respectively, while treating the third one without any perturbation as a control simulation. Thermodynamic, cloud microphysics, and precipitation budgets are then calculated from the zonally averaged and vertically integrated data at hourly intervals from these experiments. Results show the generation of larger differences in the cloud hydrometeors and surface rain rates, with the given PW perturbations. This indicates that the model-simulated clouds and precipitation are extremely sensitive to the initial errors in PW, primarily through the biased condensation process.

Citation: Li, X., S. Zhang, and D.-L. Zhang (2006), Thermodynamic, cloud microphysics, and rainfall responses to initial moisture perturbations in the tropical deep convective regime, *J. Geophys. Res.*, *111*, D14207, doi:10.1029/2005JD006968.

1. Introduction

[2] Water vapor is an important energy source for tropical convective systems. It serves as the major constituent in moist available potential energy [e.g., *Li et al.*, 2002c] and its horizontal gradient is sometimes more important than the horizontal temperature gradient in near-barotropic environments [e.g., *Gao et al.*, 2005b]. As a critical atmospheric variable, its three-dimensional (3-D) distribution in numerical models may have important implications to the prediction of clouds and precipitation. On the other hand, uncertainties in the model physics representations would produce large errors in the prediction of vertical circulations and thermodynamic structures at all spatial scales.

[3] Since 1999, NESDIS' Microwave Surface and Precipitation Products System (MSPPS) has operationally provided the retrieved precipitable water (PW, the mass-weighted mixing ratio of water vapor) from satellite-measured radiances. *Grody et al.* [2001] have validated the accuracy of the MSPPS data and the retrieved PW from NOAA 15 Advanced Microwave Sounding Unit (AMSU) against various data including radiosonde observations (RAOBs) and ground-based microwave radiometer (MWR) measurements from the Atmospheric Radiation Measurement (ARM) Tropical Western Pacific sites and Commonwealth Scientific and Industrial Research Organization (CSIRO)–maintained site at Cape Grim, Tasmania. They found good agreements between the satellite-retrieved PW and the corresponding validation data with biases ranging from 0.44 to 1.86 mm and a root-mean-square (RMS) difference of 3 mm.

[4] As an example, Figure 1a shows the horizontal distribution of PW over the global tropics. The Intertropical Convergence Zone (ITCZ) and South Pacific Convergence Zone (SPCZ) appear around the equatorial Pacific with a large amount of PW (up to 60 mm). This data set provides a great opportunity to validate the PW simulated by any global and regional model, e.g., NCEP's Global Data Assimilation System (GDAS) for the present study. For instance, a comparison of the PW field produced by GDAS and MSPPS shows that GDAS could reproduce reasonably well the basic patterns of the satellite-retrieved PW, due partly to the assimilation of the observed moisture information. However, the magnitudes of PW in both the simulated and the satellite-retrieved data differ markedly, as indicated by the collocated scatterplots in Figure 2. The RMS differences of PW between the simulated and the satellite-retrieved data are 2.5 mm over the clear-sky regions and 4.5 mm over cloudy regions. A cloudy region is defined

[1]Joint Center for Satellite Data Assimilation and National Oceanic and Atmospheric Administration/National Environmental Satellite, Data, and Information Service Center for Satellite Applications and Research, Camp Springs, Maryland, USA.
[2]Department of Atmospheric and Oceanic Science, University of Maryland, College Park, Maryland, USA.

0148-0227/06/2005JD006968$09.00

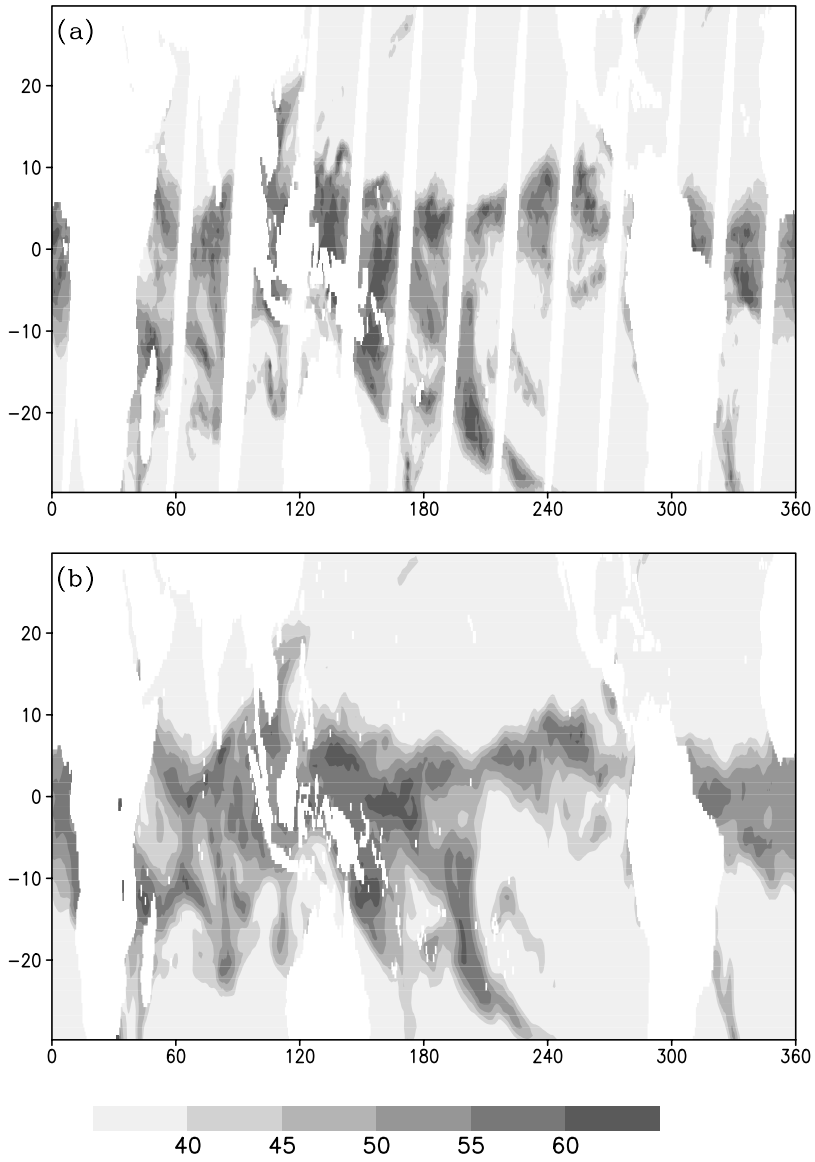

Figure 1. Horizontal distribution of precipitable water (millimeters) over the tropical region: (a) retrieved by MSPPS from NOAA 15 satellite measurements and (b) simulated by GDAS on 24 March 2003.

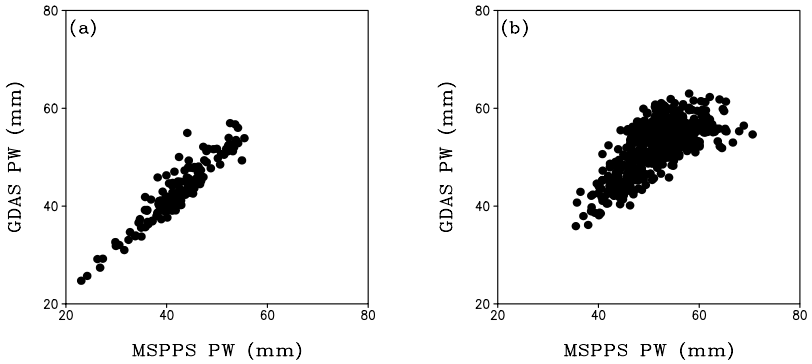

Figure 2. Scatterplots of the GDAS-simulated versus the MSPPS-retrieved PW (millimeters) in (a) clear-sky regions and (b) cloudy regions based on the area-averaged data with horizontal (latitude-longitude) resolution of $2° \times 2°$.

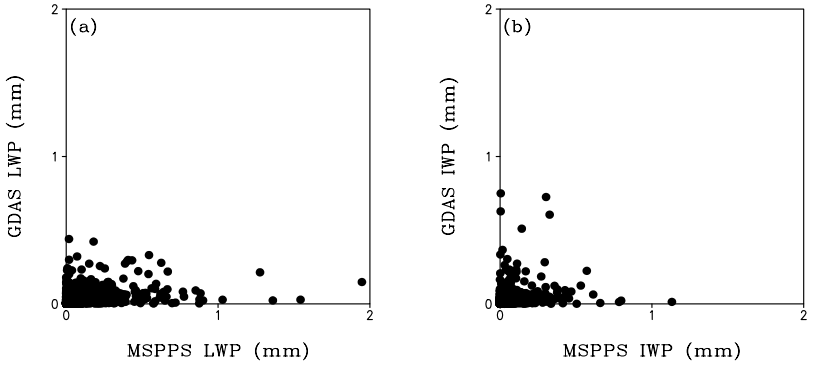

Figure 3. Scatterplots of the GDAS-simulated versus the MSPPS-retrieved (a) LWP (millimeters) and (b) IWP (millimeters) based on the horizontal (latitude-longitude) resolution of $2^\circ \times 2^\circ$ data.

herein as a region over which the sum of the mass-weighted mixing ratios of water (liquid water path; LWP) and ice (ice water path; IWP) hydrometeors is larger than 5×10^{-4} mm. The standard deviations of PW in MSPPS are 6.5 and 6.0 mm over the clear-sky and cloudy regions, respectively, as compared to the respective 6.4 and 5.1 mm in GDAS. The RMS differences of PW between MSPPS and GDAS are smaller than its standard deviations over both the clear-sky and cloudy regions. Of relevance to this study is that the RMS differences over cloudy regions are significantly greater than those over clear-sky regions. To statistically measure the PW error relative to its mean, the statistical PW error of GDAS with respect to MSPPS is calculated as the ratio of the RMS difference to its area-averaged values, and it is 42.3 (43.2) mm over the clear-sky regions and 51.7 (52.1) mm over cloudy regions in MSPPS (GDAS). The area-averaged values are calculated simply by dividing the sum of the PW data (in Figure 2) by the sample numbers, respectively, for MSPPS and GDAS over clear-sky and cloudy regions. This definition could be easily applied to the PW perturbation calculations in the experiments to be described later. Thus the PW statistical error in the GDAS product is 6% over clear-sky regions and 8.5% over cloudy regions.

[5] NESDIS' MSPPS also retrieves IWP and LWP [*Weng et al.*, 1997; *Weng and Grody*, 2000; *Zhao and Weng*, 2002; *Weng et al.*, 2003] whereas GDAS contains the predicted cloud profiles that may be used to estimate IWP and LWP. The RMS difference in nonprecipitating IWP between AMSU retrievals and ground-based radiometer measurements ranges from 0.02 to 0.08 [e.g., see *Grody et al.*, 2001]. The IWP is physically retrieved from AMSU through a two-stream radiative transfer solution [*Weng and Grody*, 2000], and its associated errors may come from the scattering parameter and uncertainties in diameter and bulk density [*Weng and Grody*, 2000; *Zhao and Weng*, 2002]. The validation of the AMSU-retrieved IWP is not available because of the scarcity of observations.

[6] By comparison, GDAS uses a prognostic cloud microphysics scheme [*Zhao and Carr*, 1997] and a cumulus parameterization scheme [*Arakawa and Schubert*, 1974] in which condensation immediately becomes precipitation falling to the ground without the presence of clouds. Thus cloud hydrometeors produced by parameterized convection would yield significantly smaller LWP ($\sim$0.5 mm) than that retrieved by MSPPS ($\sim$1–2 mm) (Figure 3a). The magnitudes of IWP in both GDAS and MSPPS are similar ($\sim$1 mm), with an RMS difference of 0.12 mm (Figure 3b). The standard deviation of IWP is 0.11 mm for MSPPS and 0.06 mm for GDAS; they are smaller than the RMS differences. In addition, the area-averaged IWP is 0.05 mm for MSPPS and 0.04 mm for GDAS, giving rise to a statistical error of more than 200% of IWP in GDAS. These results indicate that the simulated cloud field in GDAS differs significantly from the observed.

[7] Thus the purpose of this study is to determine where the large error in the simulated cloud fields is likely generated, using the satellite-retrieved data as a benchmark. Possible model errors may originate from the parameterization schemes of cloud, radiative, and subgrid-scale turbulence processes as well as the model initial conditions. In this study, we hypothesize that the above mentioned large IWP errors are closely related to the errors of PW in GDAS. To test this hypothesis, a series of experiments with three different initial conditions in PW is conducted using a two-dimensional (2-D) cloud-resolving model. The next section briefly describes the coupled model and experimental designs. Section 3 shows how small initial PW perturbations could result in large errors in the simulated cloud field. The physical processes involved as well as the thermodynamic response to the initial PW perturbations will also be discussed. A summary and concluding remarks are given in the final section.

2. Model Description and Experimental Design

[8] The cloud-resolving model used in this study was originally developed by *Soong and Ogura* [1980], *Soong and Tao* [1980], and *Tao and Simpson* [1993] and later modified by *Sui et al.* [1994, 1998] and *Li et al.* [1999]; see *Li et al.* [1999, 2002b] for its governing equations and model setup. The cloud microphysics scheme used contains five prognostic equations for mixing ratios of cloud water, rainwater, cloud ice, snow, and graupel, as documented by *Rutledge and Hobbs* [1983, 1984], *Lin et al.* [1983], *Tao et al.* [1989], and *Krueger et al.* [1995]. The other physics schemes include the solar [*Chou et al.*, 1998] and thermal infrared [*Chou et al.*, 1991; *Chou and Suarez*, 1994] radiation parameterizations that are calculated every 3 min during the model integration. The horizontal domain is

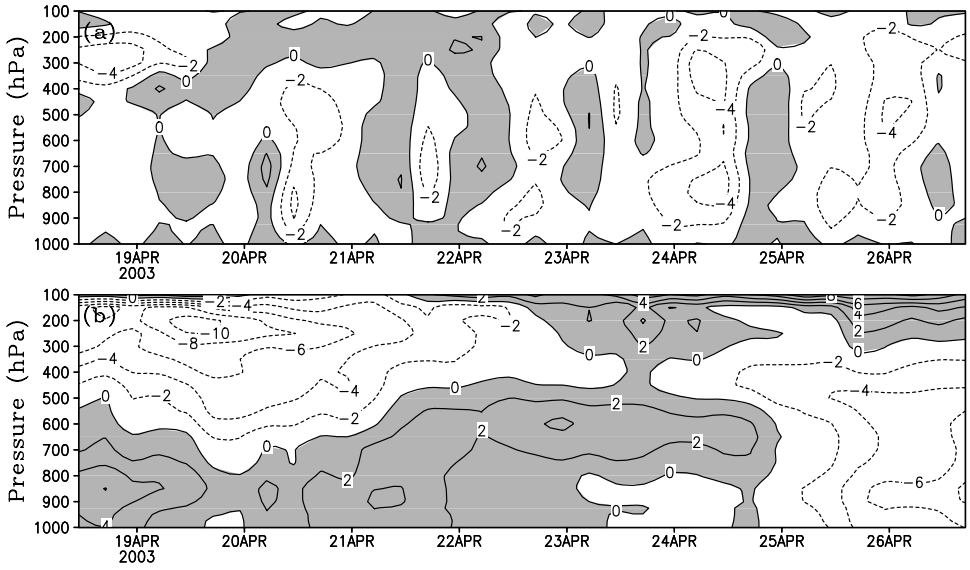

Figure 4. Time-pressure cross sections of (a) vertical motion (hPa h^{-1}) and (b) zonal wind (m s^{-1}) obtained from GDAS during the selected 8-day period. Downward motion in Figure 4a and westerly wind in Figure 4b are shaded.

768 km with a grid size of 1.5 km and periodic lateral boundary conditions. The vertical grid resolution ranges from about 200 m near the surface to about 1 km near 100 hPa; the model top is set at 42 hPa. A time step of 12 s is used. The cloud-resolving simulations have been extensively validated against observations in terms of atmospheric thermodynamic profiles, surface fluxes, and surface rain rates in the tropics during the Global Atmospheric Research Program Atlantic Tropical Experiment (GATE) [e.g., *Xu and Randall*, 1996; *Grabowski et al.*, 1996] and Tropical Ocean Global Atmosphere–Coupled Ocean Atmosphere Response Experiment (TOGA-COARE) [e.g., *Wu et al.*, 1998; *Li et al.*, 1999, 2002a, 2002b, 2002c, 2005; *Gao et al.*, 2004, 2005a, 2005b, 2006].

[9] The model is forced by zonally uniform vertical velocity, zonal wind, along with thermal and moisture advection based on 6-hourly GDAS data that are averaged over 150°–160°E, EQ, and by daily mean sea surface temperature (SST) data that are retrieved from NASA/TRMM TMI radiometer with a 10.7 GHz channel [*Wentz et al.*, 2000]. The model is integrated from 1100 LST 18 April to 1700 LST 26 April 2003 (i.e., a total of 8.25 days). Figure 4 shows the time evolution of the vertical distribution of the imposed large-scale vertical velocity and zonal wind. A period of strong ascending motion, peaked at -4 hPa h^{-1} near 300 hPa, occurs on 18 April 2003. Moderate upward motions of -2 hPa h^{-1} appear daily in the middle to lower troposphere during the period of 20–22 April when westerly winds are confined in the lower troposphere with weakening easterly flows. Two strong ascending motion centers extend from the lower to the upper troposphere on 24 and 25 April when the westerly winds switch into the intensifying easterly winds.

[10] Three experiments are designed to study the impact of initial errors in PW on the subsequent error growth in cloud hydrometeors and precipitation. Experiment C is defined as a control (true) experiment. Experiments CP and CM are identical to Experiment C except that 10% of PW is added and reduced in the model initial conditions, respectively.

[11] The temperature and moisture fields between C and GDAS are compared by calculating their RMS differences that are 0.8°C and 0.24 g kg^{-1} over vertical and horizontal model domains, respectively. These values are smaller than those between simulations and observations during TOGA-COARE [*Li et al.*, 1999].

[12] It should be noted that some cloud structures and mass circulations may not be well represented by a 2-D model. For example, *Moncrieff and Miller* [1976] showed that the 3-D crossover flow pattern associated with propagating tropical squall lines can only be simulated in the 3-D framework. In contrast, *Rotunno et al.* [1988] found that the 2-D framework captures well the basic dynamics associated with long-lived squall lines in strong low-level shear. *Sui et al.* [2005] showed the statistical equivalence between large-scale precipitation efficiency and cloud microphysics precipitation efficiency using the gridded data from both 2-D cloud-resolving simulations of tropical squall lines with the TOGA-COARE forcing and 3-D cloud-resolving simulations of typhoons without an imposed forcing. J.-J. Wang et al. (Evolution, structure, cloud microphysical and surface rainfall processes of a monsoon convection during the South China Sea Monsoon Experiment, submitted to *Journal of Atmospheric Sciences*, 2006) combined a 2-D cloud-resolving simulation with dual-Doppler and polarimetric radar analysis to study the evolution, dynamic structure, cloud microphysics, and rainfall process of a monsoon convection observed during South China Sea (SCS) summer monsoon onset, and found a good agreement between the model simulations and the radar observations. Thus the current 2-D framework should be suitable for studying the statistical properties of PW and IWP.

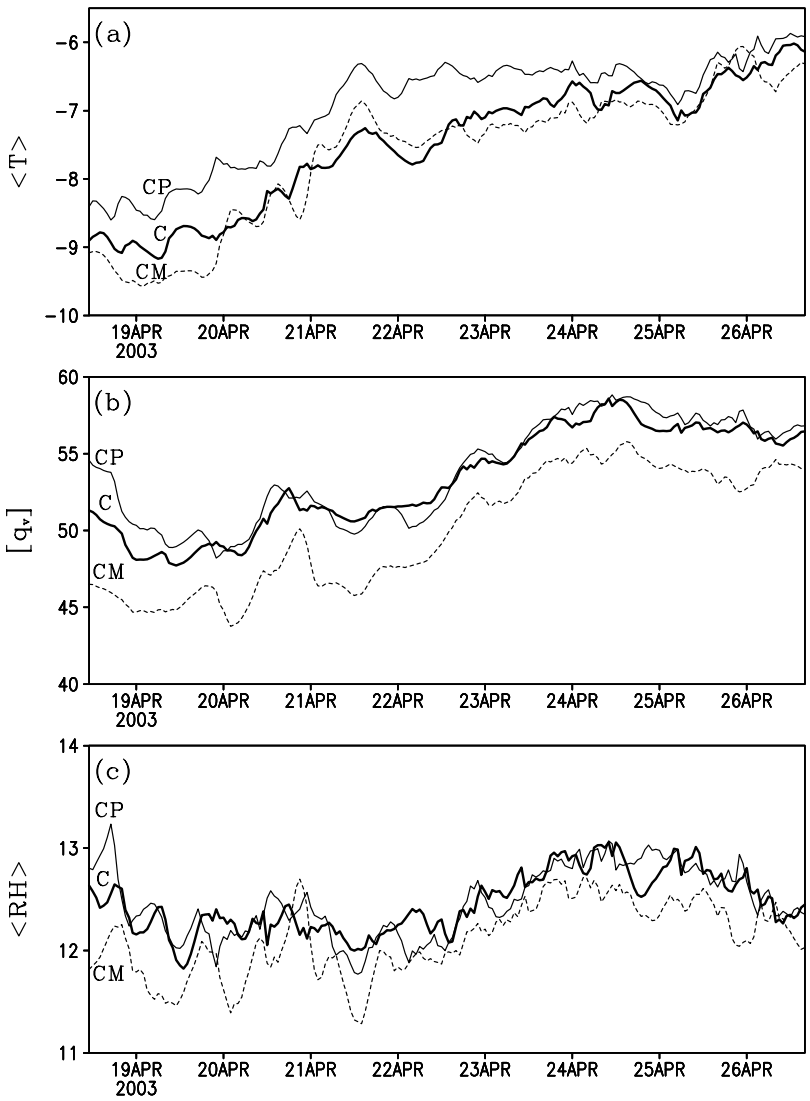

Figure 5. Time series of (a) mass-weighted mean temperature (°C), (b) precipitable water (millimeters), and (c) mass-weighted mean relative humidity (percent) during the selected 8-day period. Dark solid, light solid, and dashed lines denote experiments C, CP, and CM, respectively.

[13] The zonal mean heat budget is calculated, following *Li et al.* [1999, 2005], namely,

$$\frac{\partial \overline{T}}{\partial t} = \frac{\overline{Q}_{cn}}{c_p} + \frac{\overline{Q}_R}{c_p} - \frac{\pi}{\overline{\rho}} \frac{\partial \left(\overline{\rho} \overline{w'\theta'} \right)}{\partial z} - \pi \overline{w}^o \frac{\partial \overline{\theta}}{\partial z} - \overline{u}^o \frac{\partial \overline{T}^o}{\partial x}. \quad (1)$$

Equation (1) states that the local rate change of zonal mean temperature is determined by the terms on the right hand size (RHS) that are, respectively, condensational heating, radiative heating, convergence of vertical heat flux, vertical temperature advection, and the imposed horizontal temperature advection. The zonal mean moisture budget is

$$\frac{\partial \overline{q}_v}{\partial t} = -\overline{S}_{qv} - \frac{1}{\overline{\rho}} \frac{\partial \left(\overline{\rho} \overline{w'q'_v} \right)}{\partial z} - \overline{w}^o \frac{\partial \overline{q}_v}{\partial z} - \overline{u}^o \frac{\partial \overline{q}_v^o}{\partial x}. \quad (2)$$

Thus the local change of zonal mean water vapor is contributed by net condensation, convergence of vertical moisture flux, vertical moisture advection, as well as the imposed horizontal moisture advection.

[14] With the total conservation of vapor, cloud condensate and surface rain rate [e.g., *Ooyama*, 1990, 2001; *Bannon*, 2002], the surface rain rate is simply formulated with the sum of moisture and cloud sources/sinks. *Gao et al.* [2005a] analyzed the surface rain rate using the hourly zonal mean simulation data from a 2-D cloud-resolving model. Local moisture change, water vapor convergence (with an imposed vertical velocity) and surface evaporation contribute to the moisture sink, whereas local hydrometeor change contributes to the cloud source/sink because of the use of the cyclic boundary conditions. They found that although the moisture sink largely accounts for the variation of the surface rain rate, the cloud source/sink could modify the surface rain rate significantly. Their results indicate that the budget analysis can quantitatively identify the dominant physical processes in the surface precipitation.

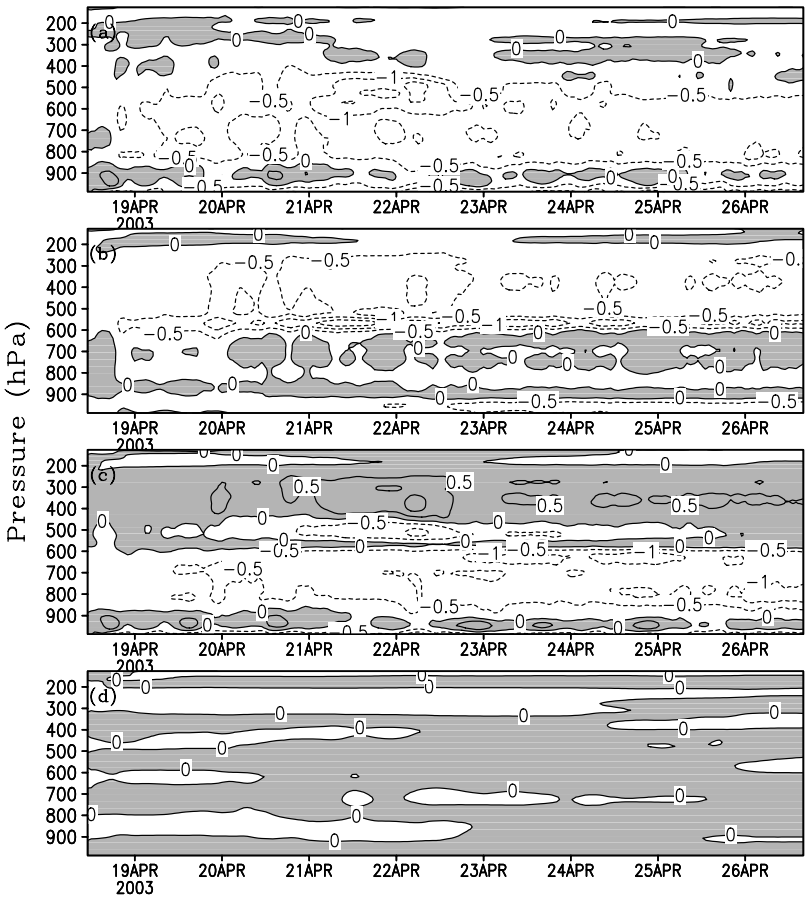

Figure 6. Time-pressure cross sections of (a) specific humidity differences between CP and C (i.e., CP-C) and their attributions to (b) condensation, (c) vertical moisture flux divergence, and (d) moisture advection. Units are in g kg^{-1}. Positive differences are shaded. The difference at 1100 LST, 18 April 2003, is removed in Figure 6a.

[15] Following *Gao et al.* [2005a], the zonal mean surface rain rate (P_s) can be symbolically expressed as

$$P_s = Q_{WVT} + Q_{WVF} + Q_{WVE} + Q_{CM}, \quad (3)$$

where $Q_{WVT} = -\partial[q_v]/\partial t$; $Q_{WVF} = -[\overline{u}^o\,(\partial\overline{q}_v^o/\partial x)] - [\overline{w}^o\,(\partial\overline{q}_v/(\partial\overline{q}_v/\partial z)]$; $Q_{WVE} = E_s$; $Q_{CM} = -\partial[q_5]/\partial t$; $(-[\overline{u}^o\,(\partial\overline{q}_v^o/\partial x)] - [\overline{w}^o\,(\partial\overline{q}_v/\partial z)]])$ is the vapor advection caused mainly by vertical moist/dry advection since the imposed horizontal vapor advection is much smaller than the vertical advection; q_v is specific humidity; E_s is surface evaporation rate; $q_5 = q_c + q_r + q_i + q_s + q_g$ is the sum of the mixing ratios of cloud water (q_c), rainwater (q_r), cloud ice (q_i), snow (q_s, density 0.1 g cm^{-3}), and graupel (q_g, density 0.4 g cm^{-3}); $-[u(\partial q_5/\partial x)] - [w(\partial q_5/\partial z)] = 0$ because of cyclic boundary conditions. Overbar denotes a zonal mean; [ ] is a zonal mean mass integration; superscript ° is an imposed observed value, and all the other variables assume their conventional meanings; similarly for all the other variables mentioned below.

[16] Following *Li et al.* [1999, 2005], the thermodynamics budget can be expressed as

$$Q_{HT} + Q_{HF} + Q_{HS} + Q_{LH} + Q_{RAD} = 0, \quad (4)$$

where $Q_{HT} = -(\partial\langle T\rangle)/\partial t$; $Q_{HF} = -\langle\overline{u}^o\,(\partial\overline{T}^o/\partial x)\rangle - \langle\pi\overline{w}^o\,(\partial\theta/\partial z)\rangle$; $Q_{HS} = H_s$; $Q_{LH} = (1/c_p)\,\langle Q_{cn}\rangle$; $Q_{RAD} = (1/c_p)\langle Q_R\rangle$; $(-\langle\overline{u}^o\,(\partial\overline{T}^o/\partial x)\rangle - \langle\pi\overline{w}^o(\partial\bar{\theta}/\partial z)\rangle)$ is the temperature advection caused mainly by vertical cold/warm advection since the imposed horizontal thermal advection is much weaker than its vertical advection; H_s is the surface sensible heat flux; $\pi = (p/p_0)^{(R/c_p)}$; Q_{cn} denotes the net latent heat release through phase changes among different cloud species; Q_R is the radiative heating rate due to convergence of net flux of solar and infrared radiative fluxes.

3. Results

[17] In this section, we will attempt to gain insight into model errors through the RMS analysis in the budgets of thermodynamics, cloud microphysics and surface rainfall. Instantaneous domain-averaged data at hourly intervals are used in the following calculations.

3.1. Thermodynamic States

[18] Figure 5 shows the time series of zonal-averaged, mass-weighted mean temperature, PW, and mass-weighted mean relative humidity in the three experiments (CP, C, and CM). Apparently, CP experiences warming and moistening whereas CM shows net cooling and drying, both relative to those in C. PW in CP approaches that in C after 1-day integration whereas the mean temperature becomes close to that in C after 5-day integrations (in the last two days). The

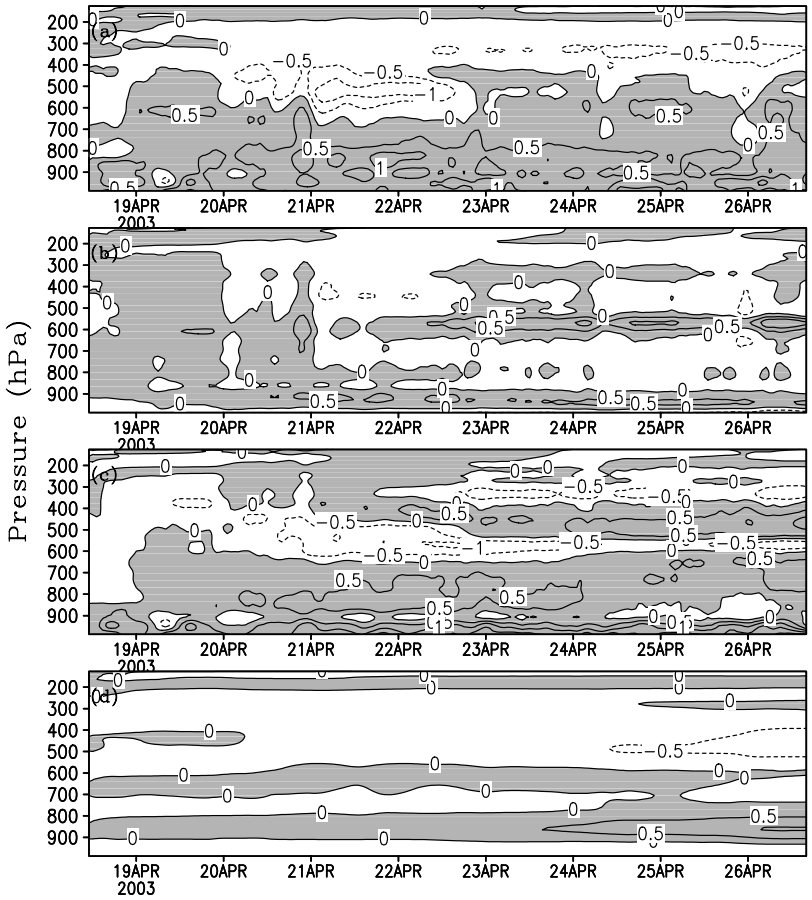

Figure 7. As in Figure 6, except for the specific humidity differences between CM and C (i.e., CM-C).

similarity between CP and C implies a cooling and drying response. The PW difference between C and CM is maintained during the integrations whereas the mean temperature in CM turns to be similar to that in C after 2-day integrations. Mass-weighted mean relative humidity in CP is similar to that in C whereas mass-weighted mean relative humidity in CM is lower than that in C (Figure 5c). The temporally averaged and domain-averaged temperature is -6.9°C in CP, -7.5°C in C, and -7.6°C in CM, whereas the corresponding averaged value of PW is 53.8 mm in CP, 53.5 mm in C, and 50.1 mm in CM.

[19] To explain the moisture and temperature differences between CP/CM and C, the differences in moisture (equation (2)) and temperature (equation (1)) budgets are analyzed. Since the moisture and temperature tendencies have large fluctuations, Equations (1) and (2) are integrated with time starting from the zero temperature and moisture difference at 1100 LST 18 April 2003 for CP, CM, and C; and the differences between CP and C (hereafter referred to as CP-C) and CM and C (CM-C) are taken to identify the dominant physical processes that are responsible for the moisture and temperature differences. Thus the q_v and temperature differences for CP-C and CM-C at 1100 LST 18 April 2003 are removed in Figures 6a and 7a and in Figures 8a and 9a, respectively.

[20] To understand the moisture difference between CP and C, the time-pressure distribution of the q_v difference between CP and C (hereafter referred to as CP-C) is shown in Figure 6a, with the contributing processes due to condensation, vertical moisture flux convergence, and vertical moisture advection given in Figures 6b–6d, respectively. The pronounced relative drying of 2 g kg^{-1} is clearly seen near 600 hPa on 22 April (Figure 6a). This drying is mainly caused by the generation of more condensation in CP (Figure 6b). This drying leads to the similarities of temporally averaged and domain-averaged PW in CP and C.

[21] Although the drying of CM relative to C (or CM-C) also appears around 600 hPa on 21–22 April (Figure 7a), the relative moistening below 700 hPa offsets the relative drying above when integrated vertically. This cancellation appears during the later days, too; so there is little moistening or drying of CM relative to C., which results in the negative difference in temporally averaged and domain-averaged PW for CM-C. Some moisture differences are present but mainly caused by differences in the vertical moisture flux convergence (compare Figures 7a and 7c), although the condensation surplus around 600 hPa (Figure 7b) and the vertical moisture advection deficit between 400 and 600 hPa during the last two days (Figure 7d) also make some contributions.

[22] Figures 8a–8e show the temperature difference between CP and C, the time-pressure distribution of the temperature difference for CP-C, and various contributing processes due to condensational heating, radiative heating, vertical heat flux convergence, and vertical temperature advection. The time-pressure distribution of temperature differences (i.e., CP-C) shows positive values above

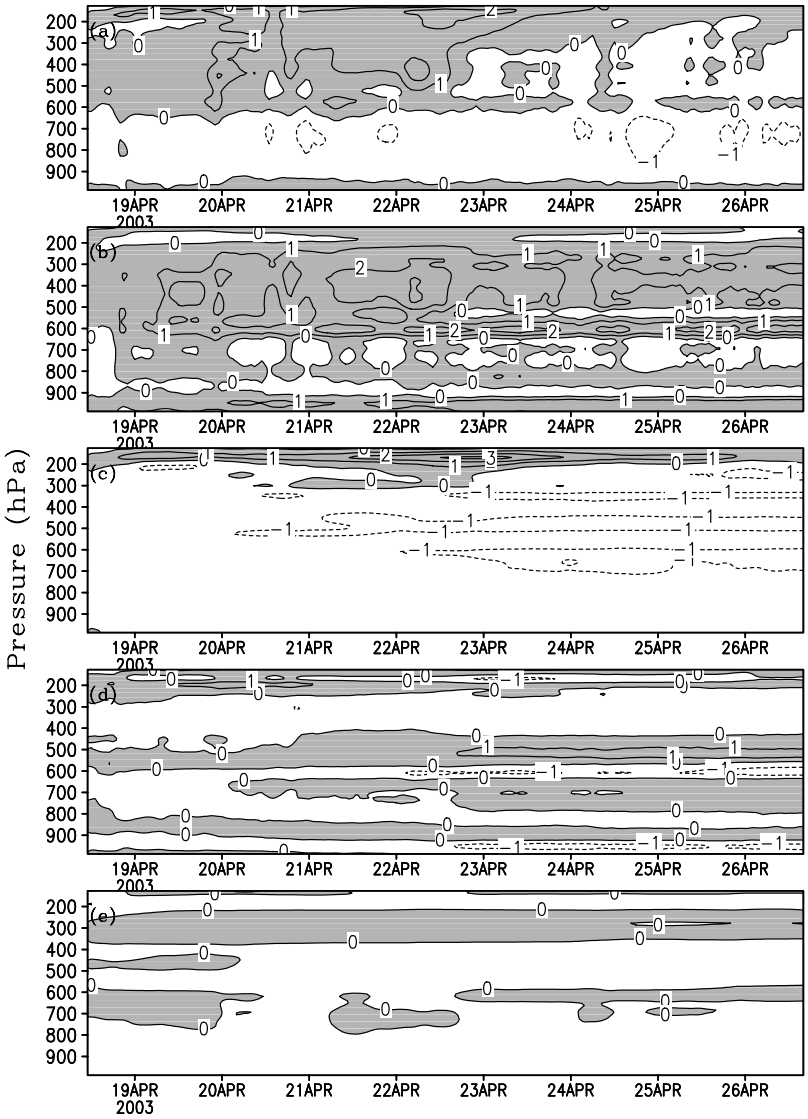

Figure 8. Time-pressure cross sections of (a) temperature differences, at intervals of 1°C, between CP and C (i.e., CP-C) and their attributions to (b) condensational heating, (c) radiative heating, (d) vertical heat flux divergence, and (e) temperature advection. Positive differences are shaded. The difference at 1100 LST, 18 April 2003, is removed in Figure 8a.

600 hPa and negative values below, leading to the vertical canceling effects, particularly during the first 6-day integrations (Figure 8a). Thus CP does not exhibit significant cooling or warming relative to C. The positive temperature difference diminishes after 6 days and relative cooling appears during the final 2 days. The positive temperature difference is mainly due to the positive difference in condensational heating (Figure 8b), whereas the negative temperature difference is mainly caused by the negative difference in radiation (Figure 8b). The effects of vertical heat flux divergence are small (Figure 8d). The negative difference in radiation strengthens with time whereas the positive difference in condensational heating weakens from 3°C to 1°C. It follows that both condensational and radiative heating are major processes causing the weakening of the positive temperature difference during the final 2-day integrations. The cancellation between the positive difference in condensational heating and the negative difference in radiative heating in the first 6-day integration is mainly responsible for the positive difference in temporally averaged and domain-averaged temperatures for CP-C.

[23] A period of negative temperature differences (i.e., CM-C) appears around 250 hPa on 18–19 April (Figure 9a), which is mainly due to the negative difference in radiation (Figure 9c). This indicates that the relative radiative cooling leads to the relative cooling in CM after 2-day integration. A positive temperature difference occurring around 400 hPa on 21–22 April (Figure 9a) that yields the relative warming in CM, is contributed by positive differences in radiation (Figure 9c) as well as condensational heating (Figure 9b). This warming offsets the negative temperature difference for CM and C after 6-hour spin-up, which leads to the similarities in temporally averaged and domain-averaged temperatures in CM and C.

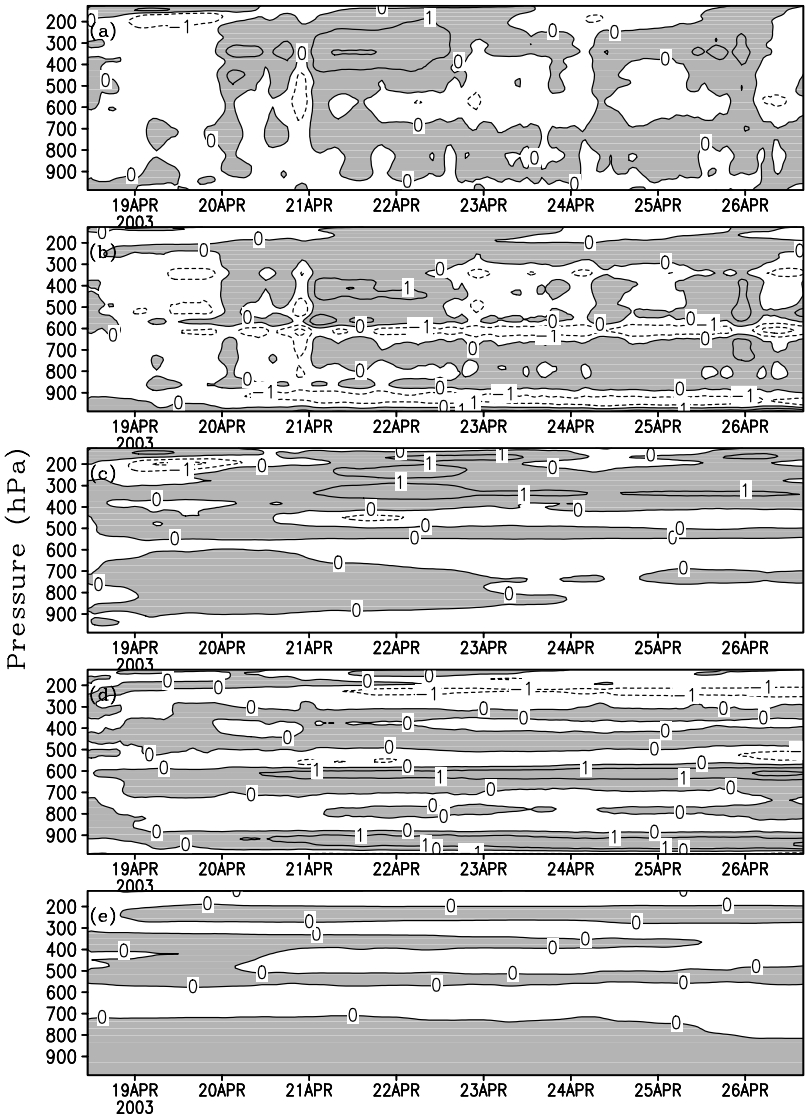

Figure 9. As in Figure 8, except for the temperature differences between CM and C (i.e., CM-C).

3.2. Cloud Hydrometeors

[24] Figure 10 shows scatterplots of CP versus C, and CM versus C for PW, IWP, and LWP. The PW simulated in CP and C appears along the diagonal line of the diagram, indicating a small RMS difference (1.1 mm) in CP-C, although the initial difference in PW is 5.1 mm. In contrast, the PW simulated in CM and C is below the diagonal line of the diagram, suggesting a large RMS difference (3.3 mm) in CM-C. Like the statistical error of GDAS, the statistical error of PW is 2.1% in CP and 6.6% in CM relative to C. The RMS difference for CP-C is much smaller than the standard deviation of CP (3.3 mm) whereas the difference for CM-C is slightly smaller than the standard deviation of CM (3.8 mm). Calculations of probability density function (PDF) for PW show that CP and C have similar PDF distributions, although their maximum PDF occurs with different amounts (Figure 11a). The PDF for PW in CM shifts significantly to lower amounts, compared to the PDF in C.

[25] A comparison of cloud hydrometeors (LWP and IWP) simulated in CP and CM to those in C shows widespread patterns that are away from the diagonal lines (Figures 10c–10f). The RMS difference in IWP for CP-C and CM-C is 0.104 and 0.107 mm, respectively. Both are larger than the standard deviations of CP (0.094 mm) and CM (0.093 mm). The statistical errors of IWP are 99% in CP and 102% in CM, indicating that small differences in PW at the initial time could produce large differences in IWP. This demonstrates that the large RMS differences in IWP between MSPPS and GDAS may be caused by the small RMS differences in PW. The scattered IWP patterns for CP versus C and CM versus C, resulting from the small PW differences, implies some uncertainties in cloud microphysics parameterization schemes that are nonlinear functions of temperature and moisture. The PDF calculations reveal that simulated IWP in the three experiments has similar PDF distributions except that lower IWP (<0.1 mm) occurs more frequently in CP and CM than in C (Figure 11b).

[26] The RMS differences in LWP for CP-C and CM-C are 0.085 and 0.096 mm, respectively, which are both

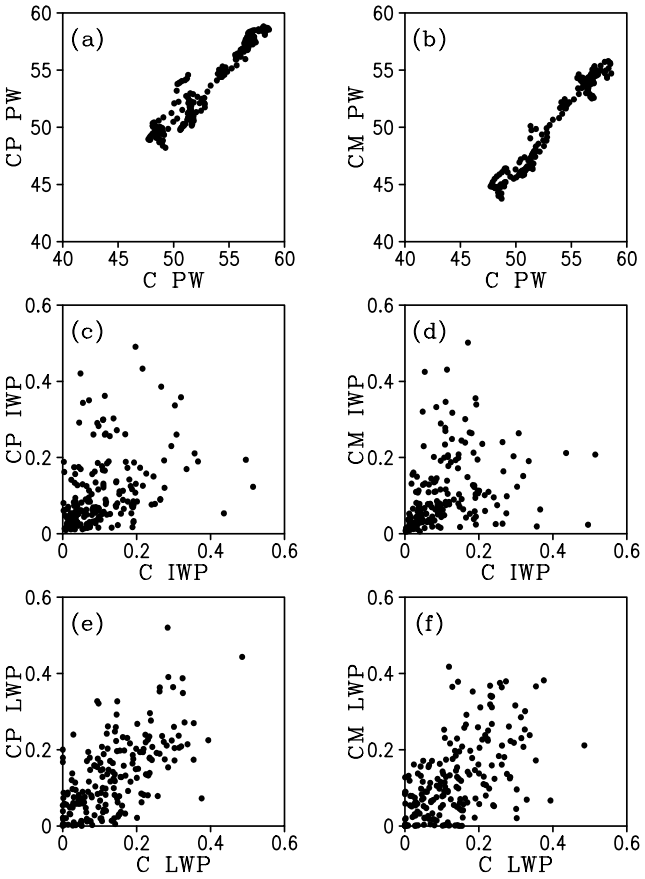

Figure 10. Scatterplots of CP versus C and of CM versus C, respectively, for zonally averaged (a and b) PW, (c and d) IWP, and (e and f) LWP. Units are in millimeters.

smaller than the standard deviations of CP (0.098 mm) and CM (0.103 mm). They give an LWP statistical error of 86.7% in CP and 93.2% in CM, which are smaller than those of IWP. Simulated IWP in the three experiments has similar PDF distributions (Figure 11c).

[27] The RMS differences in $[q_c]$, $[q_r]$, and $[q_s]$ for CP-C are 0.03, 0.064, and 0.009 mm, respectively (Figure 12), which are smaller than their corresponding standard deviations (0.034 mm in $[q_c]$, 0.069 mm in $[q_r]$, and 0.01 mm in $[q_s]$). The RMS difference in $[q_i]$ (0.011 mm) is the same as the standard deviation (0.011 mm), and for $[q_g]$ (0.092 mm) it is larger than its standard deviation (0.078 mm). In contrast, the RMS differences in $[q_r]$ and $[q_s]$ for CM-C are 0.072 and 0.009 mm, respectively, which are smaller than their corresponding standard deviations (0.076 and 0.014 mm). The RMS differences in $[q_c]$ (0.033 mm) and $[q_i]$ (0.011 mm) are slightly larger than their standard deviations (0.031 and 0.011 mm), respectively; but the RMS difference in $[q_g]$ (0.092 mm) is much larger than its standard deviation (0.077 mm). Thus it appears that large RMS differences in $[q_g]$ for CP-C and CM-C are responsible for the large RMS differences in IWP.

3.3. Surface Rainfall Processes

[28] Surface rain rates (P_s) simulated in CP and CM relative to those in C also show scattered patterns (Figures 13a and 13b). The RMS differences in P_s for CP-C and CM-C are 0.28 and 0.33 mm h^{-1}, respectively; they are similar to their standard deviations (i.e., 0.29 mm h^{-1} in CP and 0.32 mm h^{-1} in CM). They yield the P_s statistical error of 89.6% in CP and 110% in CM. Although the imposed large-scale ascending motions are identical in the three experiments, the small differences in the initial PW field still produce large differences in the surface rain rates. The PDF calculations show that the simulated surface rain rates in the three experiments have similar PDF distributions except that moderate surface rain rates ($\sim$0.5 mm h^{-1}) occur less frequently in CP and C than in C (Figure 11d).

[29] Likewise, the moisture storage rates Q_{WVT} and the hydrometeors production rates Q_{CM} for CP-C (Figures 13c and 13i) and CM-C (Figures 13d and 13j) are widespread, but the moisture convergence rates Q_{WVF} (Figures 13e and 13f) and the surface evaporation rates Q_{WVE} (Figures 13g and 13h) are well correlated. The RMS differences in Q_{WVF} ($\sim$0.01 mm h^{-1}) and Q_{WVE} ($\sim$0.02 mm h^{-1}) are significantly smaller than the standard deviations of CP (0.24 mm h^{-1}) and CM (0.04 mm h^{-1}), respectively. The small RMS difference in Q_{WVF} reflects the dominance of the imposed vertical velocity during the integrations. The RMS differences in Q_{WVT} and Q_{CM} for CP-C (0.37 and 0.27 mm h^{-1}) and CM-C (0.4 and 0.29 mm h^{-1}) are both larger than the standard deviations of CP (0.32 and 0.19 mm h^{-1}) and CM (0.3 and 0.19 mm h^{-1}), respectively. This indicates that the RMS differences in Q_{WVT} and Q_{CM} largely contribute to the RMS differences in P_s.

[30] To help understand the large RMS differences in Q_{WVT} and Q_{CM}, the PW and total cloud budgets are separately analyzed. From *Sui et al.* [2005], the two budgets can be, respectively, expressed as

$$Q_{WVT} + Q_{WVF} + Q_{WVE} = P_{CND} + P_{DEP} + P_{SDEP} + P_{GDEP} - P_{REVP} - P_{MLTS} - P_{MLTG}, \quad (5a)$$

$$Q_{CM} = P_s - P_{CND} - P_{DEP} - P_{SDEP} - P_{GDEP} + P_{REVP} + P_{MLTS} + P_{MLTG}, \quad (5b)$$

where P_{CND}, P_{DEP}, P_{SDEP}, and P_{GDEP}, representing sinks in the moisture budget, are the time rates of condensation, deposition for the growth of cloud ice, snow, and graupel, respectively; and P_{REVP}, P_{MLTS}, and P_{MLTG}, representing sources in the moisture budget, are the time rates of evaporation of rainwater, melting snow, and melting graupel, respectively.

[31] Figure 14 shows scatterplots of CP versus C and CM versus C for $[P_{CND}]$, $[P_{DEP}]$, $[P_{SDEP}]$, $[P_{GDEP}]$, $[P_{REVP}]$, $[P_{MLTS}]$, and $[P_{MLTG}]$. The standard deviations of $[P_{CND}]$ ($\sim$0.36 mm h^{-1}) are much greater than those of $[P_{DEP}]$, $[P_{SDEP}]$, $[P_{GDEP}]$, $[P_{REVP}]$, $[P_{MLTS}]$, and $[P_{MLTG}]$ ($\sim$0.06–0.12 mm h^{-1}), indicating large fluctuations in condensation rates. The RMS differences in $[P_{CND}]$ for CP-C (0.38 mm h^{-1}) and CM-C (0.41 mm h^{-1}) are larger than their standard deviations. Thus the condensational process appears to be responsible for the large RMS differences in Q_{WVT}, Q_{CM} as well as P_s.

3.4. Discussion

[32] Since the above results show that $[P_{CND}]$ accounts for large RMS differences in Q_{WVT}, Q_{CM}, and P_s for CP-C

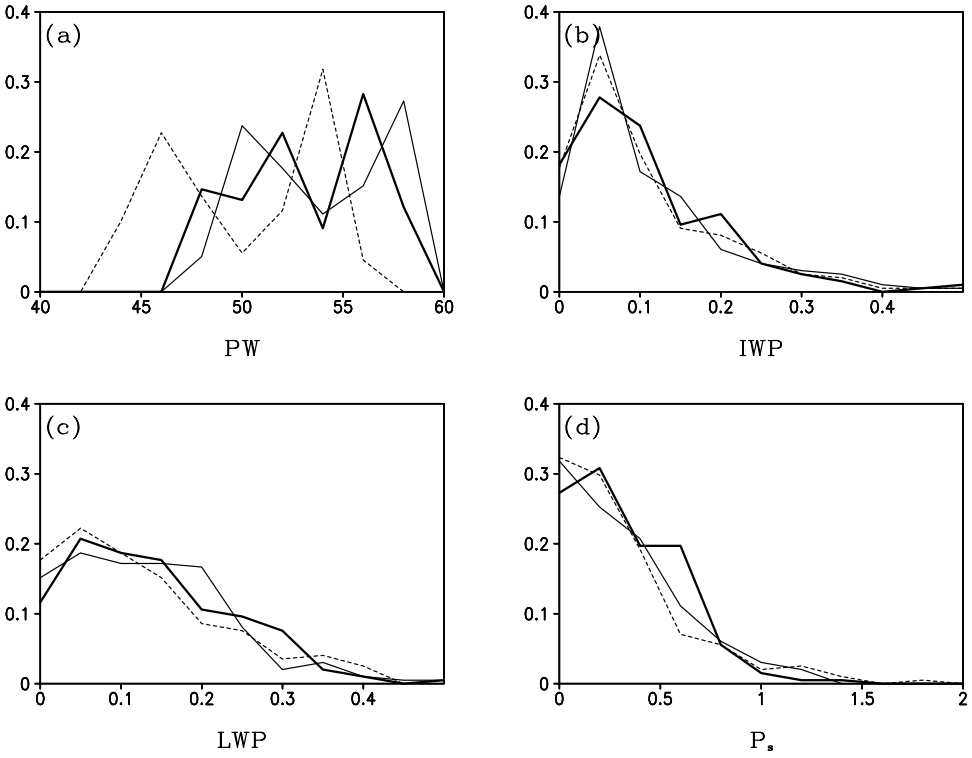

Figure 11. Probability density functions for (a) PW (millimeters), (b) IWP (millimeters), (c) LWP (millimeters), and (d) P_s (mm h^{-1}). Dark solid, light solid, and dashed lines denote experiments C, CP, and CM, respectively.

and CM-C, it is desirable to examine the production of $[P_{CND}]$ in more detail using the following equations from the cloud-resolving model of *Tao et al.* [1989],

$$P_{CND} = P_{CND1} + P_{CND2}, \tag{6a}$$

$$P_{CND1} = Cq_v, \tag{6b}$$

$$P_{CND2} = -C\left(q_{qws} + q_{is}\right), \tag{6c}$$

$$C = \frac{1}{\Delta t}\frac{T - T_{00}}{T_0 - T_{00}}\frac{1}{1 + \left(\frac{A_1 q_c q_{ws} + A_2 q_i q_{is}}{q_c + q_i}\right)\left(\frac{L_v(T - T_{00}) + L_s(T_0 - T)}{c_p(T_0 - T_{00})}\right)}, \tag{6d}$$

where $T_0 = 0°C$, T_{00} is $-35°C$; q_{ws} and q_{is} is the saturation mixing ratio with respect to water and ice, respectively; $A_1 = 237.3B_1/[(T - 35.86)^2]$; $A_2 = 265.5B_2/[(T - 7.66)^2]$; $B_1 = 17.2693882$; $B_2 = 21.8745584$; Δt is the time step.

[33] It is evident from equation (6a) that the condensation rate is primarily determined by the degree of supersaturation or subsaturation that depends nonlinearly on air temperature. This suggests that air temperature may play an important role in producing large RMS difference in $[P_{CND}]$. The RMS difference in the mean temperature for CP-C (0.63°C) is twice larger than that for CM-C (0.32°C) (see Figure 5), although both are smaller than their standard deviations (0.79°–1.01°C). Calculations of the heat budget (equation (4)) show that the RMS differences for CP-C and CM-C (see also Figure 15) are 0.01°C for Q_{RAD}, 0.09°C for Q_{HT}, 0.001°C for Q_{HF}, 0.01°C for Q_{HS}, and 0.09°C for Q_{LH}, indicating that the RMS differences in condensational heating account for those in the heat storage rates. Note that the RMS differences in Q_{HT} and Q_{LH} are greater than the standard deviations (0.07°C for Q_{HT} and 0.08°C for Q_{LH}).

[34] As indicated by equation (6a), $[P_{CND}]$ can be divided into $[P_{CND1}]$ and $[P_{CND2}]$ whose variations are associated with specific humidity and saturated specific humidity, respectively. Figure 16 shows that $[P_{CND1}]$ and $[P_{CND2}]$ are negatively correlated with similar magnitudes of about 3×10^3 mm h^{-1} in all the three experiments, whereas $[P_{CND}]$ has a magnitude of about 2 mm h^{-1} (see Figure 14). Thus the condensation rate is a small residual between the two large terms related to q_v and q_{vs}. Furthermore, the $[P_{CND}]$ variance for CP-C and CM-C can be estimated to examine sources for the errors. They are calculated by

$$\begin{aligned} Var\left(P_{CND,CP}, P_{CND,C}\right) = {} & Var\left(P_{CND1,CP}, P_{CND1,C}\right) + 2CoVar \\ & \cdot \left(P_{CND1,CP} - P_{CND1,C}, P_{CND2,CP} \right. \\ & \left. - P_{CND2,C}\right) + Var\left(P_{CND2,CP}, P_{CND2,C}\right), \end{aligned} \tag{7a}$$

$$Var\left(P_{CND,CP}, P_{CND,C}\right) = \frac{1}{n}\left(P_{CND,CP} - P_{CND,C}\right)^2, \tag{7b}$$

$$Var\left(P_{CND1,CP}, P_{CND1,C}\right) = \frac{1}{n}\left(P_{CND1,CP} - P_{CND1,C}\right)^2 \tag{7c}$$

$$\begin{aligned} & CoVar\left(P_{CND1,CP} - P_{CND1,C}, P_{CND2,CP} - P_{CND2,C}\right) \\ & = \frac{1}{n}\left(P_{CND1,CP} - P_{CND1,C}\right)\left(P_{CND2,CP} - P_{CND2,C}\right), \end{aligned} \tag{7d}$$

$$Var\left(P_{CND2,CP}, P_{CND2,C}\right) = \frac{1}{n}\left(P_{CND2,CP} - P_{CND2,C}\right)^2. \tag{7e}$$

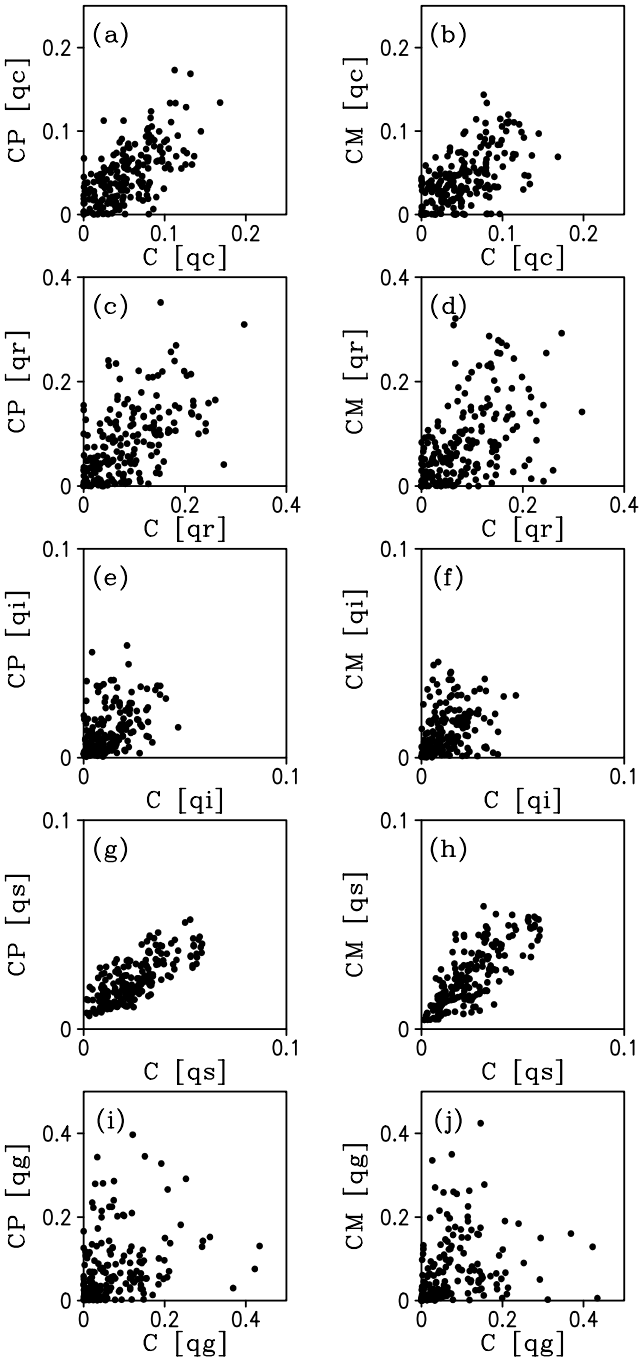

Figure 12. Scatterplots of CP versus C and of CM versus C, respectively, for zonally averaged (a and b) cloud water [q_c], (c and d) rainwater [q_r], (e and f) cloud ice [q_i], (g and h) snow [q_s], and (i and j) graupel [q_g]. Units are in millimeters.

It is found that Var($P_{CND,CP}$, $P_{CND,C}$), Var($P_{CND1,CP}$, $P_{CND1,C}$), CoVar($P_{CND1,CP} - P_{CND1,C}$, $P_{CND2,CP} - P_{CND2,C}$), and Var($P_{CND2,CP}$, $P_{CND2,C}$) are 0.142, 3151.803, −6304.007, and 3152.346 mm^2 h^{-2}, respectively. Var($P_{CND,CM}$, $P_{CND,C}$), Var($P_{CND1,CM}$, $P_{CND1,C}$), CoVar($P_{CND1,CM} - P_{CND1,C}$, $P_{CND2,CM} - P_{CND2,C}$), and Var($P_{CND2,CM}$, $P_{CND2,C}$) are 0.167, 26,395.184, −52,792.895, and 26,397.871 mm^2 h^{-2}, respectively. The variances in [P_{CND}] for CP-C and CM-C are 4–5 orders of magnitudes smaller than the variances in [P_{CND1}] and [P_{CND2}] as well as the covariances for CP-C and CM-C, implying that small perturbations in specific humidity and saturated specific humidity could cause large differences in [P_{CND}].

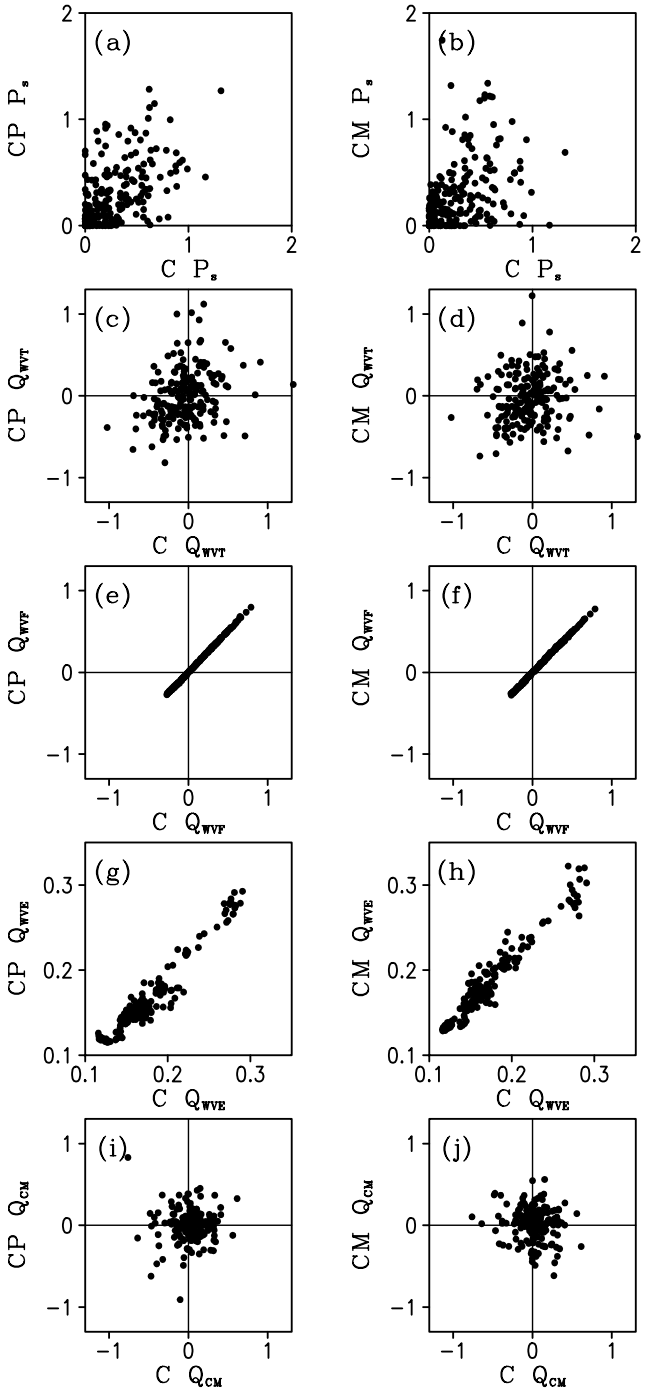

Figure 13. Scatterplots of CP versus C and of CM versus C, respectively, for (a and b) surface rainfall rates P_s, (c and d) domain-averaged moisture storage Q_{WVT}, (e and f) moisture divergence Q_{WVF}, (g and h) surface evaporation Q_{WVE}, and (i and j) hydrometeor production Q_{CM}. Units are in mm h^{-1}.

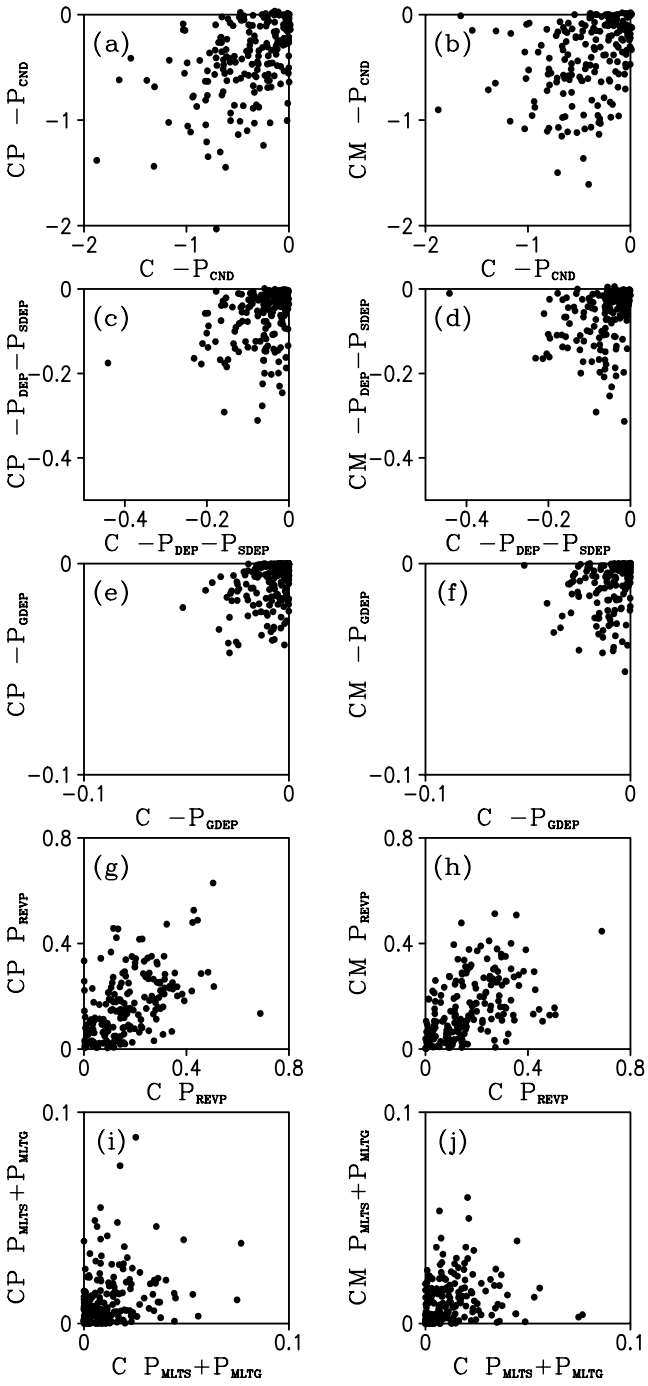

Figure 14. Scatterplots of CP versus C and of CM versus C, respectively, for (a and b) – [P_{CND}], (c and d) – [P_{DEP}] – [P_{SDEP}], (e and f) – [P_{GDEP}], (g and h) [P_{REVP}], and (i and j) [P_{MLTS}] + [P_{MLTG}]. Units are in mm h^{-1}.

[35] The above analysis suggests that the improvement of cloud simulations may rely on the reduced errors in the initial conditions or the accurate calculation of condensation rates that is sensitive to the errors in the initial conditions. Experiment CP shows that the small difference in PW during the integration can produce large differences in the simulated cloud field. Thus improving the calculation of cloud condensation may be an important way to improve cloud simulations.

4. Summary and Concluding Remarks

[36] Because of the scarcity of high-resolution observations over the tropical regions, cloud simulations have been seldom evaluated. The precipitable water (PW), ice (IWP)

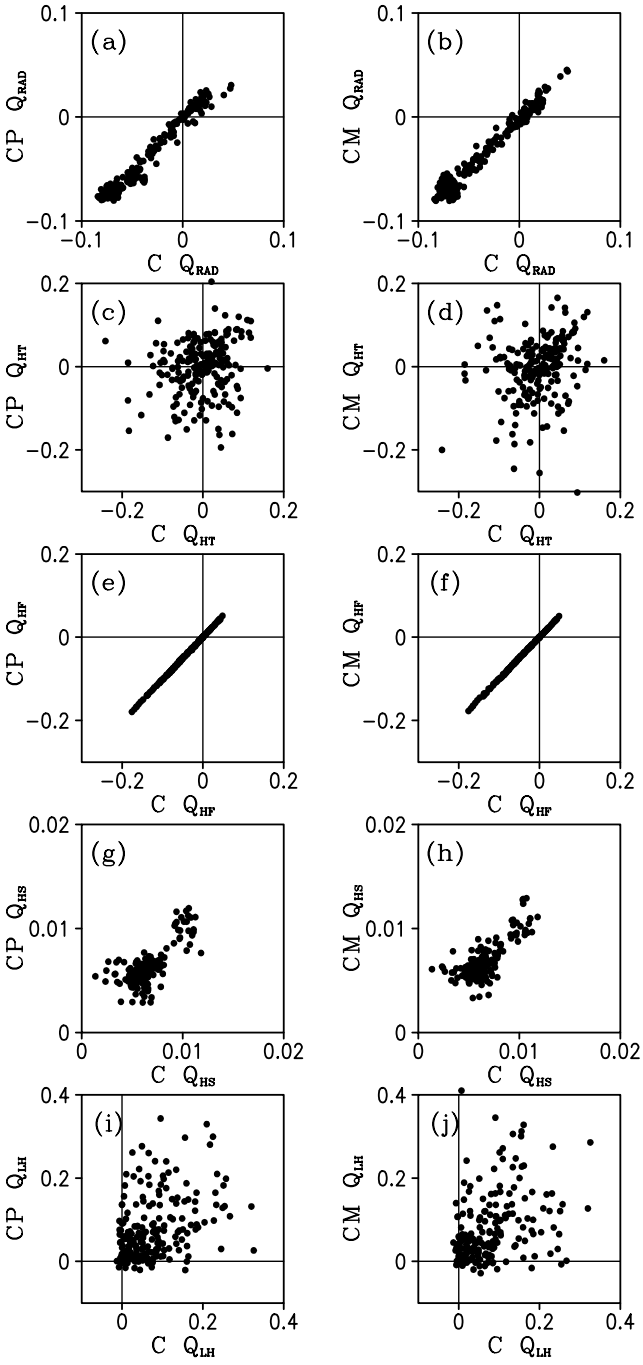

Figure 15. Scatterplots of CP versus C and of CM versus C, respectively, for (a and b) radiation Q_{RAD}, (c and d) heat storage Q_{HT}, (e and f) heat divergence Q_{HF}, (g and h) sensible heat flux Q_{HS}, (i and j) latent heat Q_{LH}. Units are in °C h^{-1}.

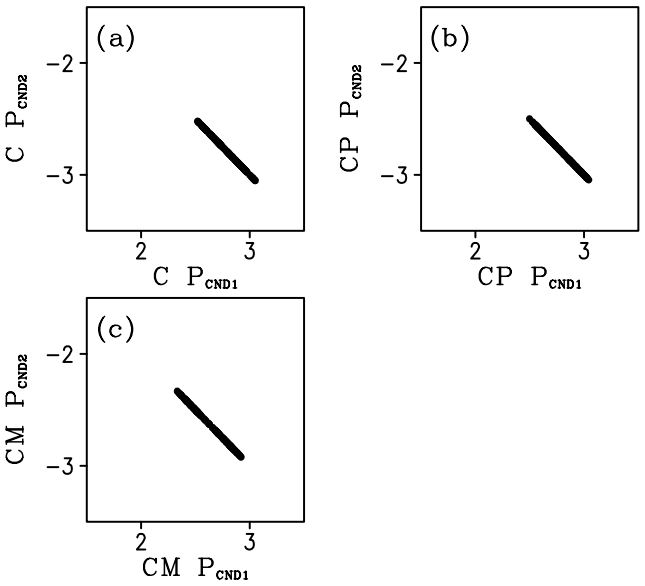

Figure 16. Scatterplots of [P_{CND1}] versus [P_{CND2}] in (a) C, (b) CP, and (c) CM. Units are in 10^3 mm h^{-1}.

and liquid (LWP) water paths from NOAA/Microwave Surface and Precipitation Products System (MSPPS) have recently been available to the public with the horizontal resolutions of 0.5° × 0.5°. Comparisons of PW and IWP between NCEP's Global Data Assimilation System (GDAS) and MSPPS reveal small differences in PW but large differences in IWP. To examine why such large differences in cloud hydrometeors between the simulation and observation are generated, three experiments are conducted with a two-dimensional cloud-resolving model in which the large-scale vertical velocity and zonal wind from NCEP's GDAS are imposed. In two of the experiments, the model initial PW field is perturbed by ±10%, respectively, while treating the third one as a control experiment. Thermodynamic, cloud microphysical and precipitation budgets are then calculated using the zonally averaged, vertically integrated simulation data at hourly intervals from three experiments.

[37] It is shown that adding 10% of PW into the model initial condition (CP) produces warming and moistening in the model atmosphere relative to the control experiment (C), after the first 6-hour spin-up, whereas the opposite scenarios occur when the initial PW field is reduced by 10% (CM). Subsequently, CP (CM) experiences drying (warming) during early days and cooling (little changes) during later days. The analysis of the mass-weighted heat and PW budgets show that more condensation and radiative cooling account for the drying and cooling during early days, respectively. More radiative cooling is responsible for the cooling during later days. Vertical moisture flux convergence shows less convergence in the upper troposphere and more convergence in the low troposphere that leads to vertical cancellation, which determines little change in moisture during later days.

[38] The large differences in the surface rain rates and the simulated cloud fields are shown to be related to the small moisture perturbations in the model initial conditions, indicating that the initial PW perturbations are one of the factors that are responsible for variations in cloud and precipitation simulations. Further analysis shows that the biased simulations occur through the condensation process, since the condensation rate is a small residual between the two large terms (i.e., q_v and q_{vs}). Thus we may conclude that accurate simulations of clouds and precipitation may hinge upon the improvement of calculating condensation and depositional growth.

[39] **Acknowledgments.** The authors wish to thank W.-K. Tao of NASA Goddard Space Flight Center and C.-H. Sui of National Central University of Taiwan for the use of their 2-D cloud-resolving model. Thanks also go to F. Weng, R. R. Ferraro, and H. Meng of NOAA/NESDIS for providing the MSPPS data, to Y. Zhu at NCEP/EMC for providing the GDAS data, and to two anonymous reviewers whose comments helped improve the manuscript significantly. This study was supported by the Joint Center for Satellite Data Assimilation. The views, opinions, and findings contained in this report are those of the author(s) and should not be construed as an official National Oceanic and Atmospheric Administration or U.S. Government position, policy, or decision.

References

Arakawa, A., and W. H. Schubert (1974), Interaction of a cumulus cloud ensemble with the large-scale environment, Part I, *J. Atmos. Sci.*, *31*, 674–701.

Bannon, P. R. (2002), Theoretical foundations for models of moist convection, *J. Atmos. Sci.*, *59*, 1967–1982.

Chou, M.-D., and M. J. Suarez (1994), An efficient thermal infrared radiation parameterization for use in general circulation models, *NASA Tech. Memo.*, *TM-1999-104606*, vol. 3, 85 pp.

Chou, M.-D., D. P. Kratz, and W. Ridgway (1991), Infrared radiation parameterization in numerical climate models, *J. Clim.*, *4*, 424–437.

Chou, M.-D., M. J. Suarez, C.-H. Ho, M. M.-H. Yan, and K.-T. Lee (1998), Parameterizations for cloud overlapping and shortwave single scattering properties for use in general circulation and cloud ensemble models, *J. Atmos. Sci.*, *55*, 201–214.

Gao, S., F. Ping, X. Li, and W. Tao (2004), A convective vorticity vector associated with tropical convection: A two-dimensional cloud-resolving modeling study, *J. Geophys. Res.*, *109*, D14106, doi:10.1029/2004JD004807.

Gao, S., X. Cui, Y. Zhou, and X. Li (2005a), Surface rainfall processes as simulated in a cloud-resolving model, *J. Geophys. Res.*, *110*, D10202, doi:10.1029/2004JD005467.

Gao, S., X. Cui, Y. Zhou, X. Li, and W. Tao (2005b), A modeling study of moist and dynamic vorticity vectors associated with two-dimensional tropical convection, *J. Geophys. Res.*, *110*, D17104, doi:10.1029/2004JD005675.

Gao, S., F. Ping, and X. Li (2006), Cloud microphysical processes associated with the diurnal variations of tropical convection: A 2D cloud resolving modeling study, *Meteorol. Atmos. Phys.*, *91*, 9–16.

Grabowski, W. W., X. Wu, and M. W. Moncrieff (1996), Cloud-resolving model of tropical cloud systems during Phase III of GATE. Part I: Two-dimensional experiments, *J. Atmos. Sci.*, *53*, 3684–3709.

Grody, N., J. Zhao, R. Ferraro, F. Weng, and R. Boers (2001), Determination of precipitable water and cloud liquid water over oceans from the NOAA 15 advanced microwave sounding unit, *J. Geophys. Res.*, *106*(D3), 2943–2953.

Krueger, S. K., Q. Fu, K. N. Liou, and H.-N. S. Chin (1995), Improvement of an ice-phase microphysics parameterization for use in numerical simulations of tropical convection, *J. Appl. Meteorol.*, *34*, 281–287.

Li, X., C.-H. Sui, K.-M. Lau, and M.-D. Chou (1999), Large-scale forcing and cloud-radiation interaction in the tropical deep convective regime, *J. Atmos. Sci.*, *56*, 3028–3042.

Li, X., C.-H. Sui, and K.-M. Lau (2002a), Precipitation efficiency in the tropical deep convective regime: A 2-D cloud resolving modeling study, *J. Meteorol. Soc. Jpn.*, *80*, 205–212.

Li, X., C.-H. Sui, and K.-M. Lau (2002b), Dominant cloud microphysical processes in a tropical oceanic convective system: A 2-D cloud resolving modeling study, *Mon. Weather Rev.*, *130*, 2481–2491.

Li, X., C.-H. Sui, and K.-M. Lau (2002c), Interactions between tropical convection and its environment: An energetics analysis of a 2-D cloud resolving simulation, *J. Atmos. Sci.*, *59*, 1712–1722.

Li, X., C.-H. Sui, K.-M. Lau, and W.-K. Tao (2005), Tropical convective responses to microphysical and radiative processes: A 2D cloud-resolving modeling study, *Meteorol. Atmos. Phys.*, *90*, 245–259.

Lin, Y.-L., R. D. Farley, and H. D. Orville (1983), Bulk parameterization of the snow field in a cloud model, *J. Clim. Appl. Meteorol.*, *22*, 1065–1092.

Moncrieff, M. W., and M. J. Miller (1976), The dynamics and simulation of tropical cumulonimbus and squall line, *Q. J. R. Meteorol. Soc.*, *102*, 373–394.

Ooyama, K. V. (1990), A thermodynamic foundation for modeling the moist atmosphere, *J. Atmos. Sci.*, *47*, 2580–2593.

Ooyama, K. V. (2001), A dynamic and thermodynamic foundation for modeling the moist atmosphere with parameterized microphysics, *J. Atmos. Sci.*, *58*, 2073–2102.

Rotunno, R., J. B. Klemp, and M. L. Weisman (1988), A theory for strong, long-lived squall lines, *J. Atmos. Sci.*, *45*, 463–485.

Rutledge, S. A., and P. V. Hobbs (1983), The mesoscale and microscale structure and organization of clouds and precipitation in midlatitude cyclones. Part VIII: A model for the "seeder-feeder" process in warm-frontal rainbands, *J. Atmos. Sci.*, *40*, 1185–1206.

Rutledge, S. A., and P. V. Hobbs (1984), The mesoscale and microscale structure and organization of clouds and precipitation in midlatitude cyclones. Part XII: A diagnostic modeling study of precipitation development in narrow cold-frontal rainbands, *J. Atmos. Sci.*, *41*, 2949–2972.

Soong, S. T., and Y. Ogura (1980), Response of tradewind cumuli to large-scale processes, *J. Atmos. Sci.*, *37*, 2035–2050.

Soong, S. T., and W. K. Tao (1980), Response of deep tropical cumulus clouds to mesoscale processes, *J. Atmos. Sci.*, *37*, 2016–2034.

Sui, C.-H., K.-M. Lau, W.-K. Tao, and J. Simpson (1994), The tropical water and energy cycles in a cumulus ensemble model, Part I: Equilibrium climate, *J. Atmos. Sci.*, *51*, 711–728.

Sui, C.-H., X. Li, and K.-M. Lau (1998), Radiative-convective processes in simulated diurnal variations of tropical oceanic convection, *J. Atmos. Sci.*, *55*, 2345–2359.

Sui, C.-H., X. Li, M.-J. Yang, and H.-L. Huang (2005), Estimation of oceanic precipitation efficiency in cloud models, *J. Atmos. Sci.*, *62*, 4358–4370.

Tao, W.-K., and J. Simpson (1993), The Goddard Cumulus Ensemble model. Part I: Model description, *Terr. Atmos. Oceanic Sci.*, *4*, 35–72.

Tao, W.-K., J. Simpson, and M. McCumber (1989), An ice-water saturation adjustment, *Mon. Weather Rev.*, *117*, 231–235.

Weng, F., and N. C. Grody (2000), Retrieval of ice cloud parameters using a microwave imaging radiometer, *J. Atmos. Sci.*, *57*, 1069–1081.

Weng, F., N. C. Grody, R. Ferraro, A. Basist, and D. Forsyth (1997), Cloud liquid water climatology from the Special Sensor Microwave/Imager, *J. Clim.*, *10*, 1086–1098.

Weng, F., L. Zhao, R. R. Ferraro, G. Poe, X. Li, and N. C. Grody (2003), Advanced microwave sounding unit cloud and precipitation algorithms, *Radio Sci.*, *38*(4), 8068, doi:10.1029/2002RS002679.

Wentz, F. J., C. Gentemann, D. Smith, and D. Chelton (2000), Satellite measurements of sea surface temperature through clouds, *Science*, *288*, 847–850.

Wu, X., W. W. Grabowski, and M. W. Moncrieff (1998), Long-term evolution of cloud systems in TOGA COARE and their interactions with radiative and surface processes. Part I: Two-dimensional cloud-resolving model, *J. Atmos. Sci.*, *55*, 2693–2714.

Xu, K.-M., and D. A. Randall (1996), Explicit simulation of cumulus ensembles with the GATE Phase III data: Comparison with observations, *J. Atmos. Sci.*, *53*, 3710–3736.

Zhao, L., and F. Weng (2002), Retrieval of ice cloud parameters using the advanced microwave sounding unit (AMSU), *J. Appl. Meteorol.*, *41*, 384–395.

Zhao, Q., and F. H. Carr (1997), A prognostic cloud scheme for operational NWP models, *Mon. Weather Rev.*, *125*, 1931–1953.

X. Li, NOAA/NESDIS/ORA, 5200 Auth Road, Room 712, Camp Springs, MD 20746, USA. (xiaofan.li@noaa.gov)

D.-L. Zhang and S. Zhang, Department of Atmospheric and Oceanic Science, University of Maryland, College Park, MD 20742, USA.